Title

Modal focal adaptive optics for Bessel-focus two-photon fluorescence microscopy.

Journal

Optics Express, 33(1)

ISSN

1094-4087

Authors

Kim, Hyeonggeon

Natan, Ryan

Chen, Wei

et al.

Publication Date

2025-01-13

DOI

10.1364/oe.541033

Research Article Vol. 33, No. 1 / 13 Jan 2025 / Optics Express 680
Optics EXPRESS

Modal focal adaptive optics for Bessel-focus two-photon fluorescence microscopy

HYEONGGEON KIM,[1] RYAN NATAN,[2,3] WEI CHEN,[2,8] AMY M. WINANS,[3] JIANG LAN FAN,[4,5] EHUD ISACOFF,[3,6,7] AND NA JI[2,3,6,7,*]

[1]Graduate Group in Applied Science and Technology, University of California, Berkeley, CA, USA
[2]Department of Physics, University of California, Berkeley, CA, USA
[3]Department of Molecular and Cell Biology, University of California, Berkeley, CA, USA
[4]Joint Bioengineering Graduate Program, University of California, Berkeley, CA, USA
[5]Joint Bioengineering Graduate Program, University of California, San Francisco, CA, USA
[6]Helen Wills Neuroscience Institute, University of California, Berkeley, CA, USA
[7]Molecular Biophysics and Integrated Bioimaging Division, Lawrence Berkeley National Laboratory, Berkeley, CA, USA
[8]Present address: School of Mechanical Science and Engineering – Advanced Biomedical Imaging Facility, Huazhong University of Science and Technology, Wuhan, China
[*]jina@berkeley.edu

Abstract: Adaptive optics (AO) improves the spatial resolution of microscopy by correcting optical aberrations. While its application has been well established in microscopy modalities utilizing a circular pupil, its adaptation to systems with non-circular pupils, such as Bessel-focus two-photon fluorescence microscopy (2PFM) with an annular pupil, remains relatively uncharted. Herein, we present a modal focal AO (MFAO) method for Bessel-focus 2PFM. Measuring and correcting aberration using a spatial light modulator placed in conjugation with the focal plane of the microscope objective, MFAO employs Zernike annular polynomials — a first in AO implementation — to achieve performance on par with a previous zonal AO method, but with a notably simplified optical configuration. We validated the performance of MFAO in correcting artificial and sample-induced aberrations, as well as in *in vivo* imaging of zebrafish larvae and mouse brains. By expanding the application of modal AO to annular pupils as well as aberration measurement and correction to a wavefront modulator at the objective focal plane, MFAO represents a notable advancement in the implementation of AO in microscopy.

1. Introduction

Two-photon fluorescence microscopy (2PFM) [1] is an indispensable tool for probing biological structure and function deep inside living organisms. By exploiting the nonlinearity of two-photon absorption and the penetration capability of near-infrared excitation wavelengths, 2PFM could achieve high-resolution, optically sectioned imaging deep within scattering tissues [2]. Conventional 2PFM utilizes a Gaussian excitation focus that is highly localized in three dimensions (3D) to achieve high spatial resolution both laterally and axially. However, during volumetric imaging, a Gaussian focus has to be scanned in 3D, substantially limiting the sampling rate [3]. In contrast, Bessel-focus 2PFM overcomes this challenge by using an axially elongated Bessel excitation focus. When scanned in two dimensions (2D) within sparsely labeled fluorescent samples, a Bessel focus produces projections of the 3D structures within its axial span at high lateral resolution [4–9]. Probing volumes at 2D frame rates, Bessel-focus 2PFM has substantially enhanced temporal resolution and has been applied to *in vivo* volumetric imaging of zebrafish larvae [8,10] and the mouse brain [8,9,11–13].

#541033 https://doi.org/10.1364/OE.541033
Journal © 2025 Received 11 Sep 2024; revised 2 Dec 2024; accepted 9 Dec 2024; published 7 Jan 2025

Optics EXPRESS

However, optical microscopy — including Gaussian-focus 2PFM and Bessel-focus 2PFM — suffers from system and sample-induced optical aberrations. These aberrations arise from imperfections and misalignments in optical components, inhomogeneity of refractive indices in biological tissue, and refractive mismatch between the sample and the immersion medium. Such aberrations can significantly impair focus quality, compromising spatial resolution as well as reducing signal and contrast. For example, for a Bessel focus, aberrations redistribute energy from its central peak to its side rings, thereby reducing the effective lateral resolution and increasing side-ring background fluorescence [14]. To mitigate these detrimental effects, various adaptive optics (AO) techniques have been implemented to correct optical aberrations in microscopy [15–17]. AO typically involves two steps: measuring the aberration and then correcting it using a wavefront modulator such as deformable mirrors or liquid-crystal spatial light modulators (SLMs). Aberration measurement may be conducted through either direct wavefront sensing (e.g., with a Shack-Hartmann sensor) or indirect methods that infer aberrations from images/signals acquired from the sample without using a wavefront sensor [18]. Indirect AO methods include zonal approach [19,20], which segment the wavefront into discrete zones, and modal approaches [21,22], which represent the wavefront as the summation of orthogonal basis sets (e.g., Zernike polynomials). Although indirect AO methods are often slower than direct AO methods, they are well-suited for wavefront sensing in highly scattering scenarios, such as when sensing deep within opaque biological tissues.

For 2PFM, AO correction of aberration is required for the excitation light [18]. While several AO approaches have been developed for conventional Gaussian-focus 2PFM [19,22–26], only recently was an AO method developed for Bessel-focus 2PFM [14], where a zonal aberration measurement method [19] used a liquid-crystal SLM placed in conjugation with the objective rear pupil plane to measure the aberration experienced by a Gaussian focus. The measured pupil aberration was subsequently used to compute the phase profile, which was then applied to another liquid-crystal SLM placed in conjugation to the objective focal plane, in order to generate a Bessel focus with the appropriate phase and amplitude profiles for aberration correction. Since the wavefront shaping for aberration correction was achieved by the SLM conjugated to the objective focal plane, we described this method as a focal AO method (in contrast to pupil AO methods, the more common approaches of placing the wavefront modulator in conjugation with the objective rear pupil plane). However, because aberration measurement and correction are performed with different SLMs conjugated to the focal and pupil-conjugated planes, respectively, this zonal focal AO (ZFAO) method demands precise optical alignment between the two SLMs and may suffer from non-common path errors [27].

In this paper, we describe a modal approach that utilizes a single SLM placed in conjugation with the objective focal plane for both aberration measurement and correction of Bessel-focus 2PFM. By dispensing with the additional SLM, our modal focal AO (MFAO) method utilizes the same optical path as a conventional Bessel-focus 2PFM and circumvents non-common path issues. Employing Zernike annular modes for wavefront representation, MFAO represents what is to our knowledge, the first experimental application of modal AO for Bessel-focus 2PFM. We demonstrate the effectiveness of our approach for correcting both system and sample-induced optical aberrations. Furthermore, we show that MFAO improves *in vivo* imaging of zebrafish larvae and mouse brains.

2. Methods

2.1. AO Bessel-focus two-photon fluorescence microscope

The MFAO approach for Bessel-focus 2PFM was implemented on the same homebuilt Bessel-focus 2PFM system (Fig. 1(a)) as the previous ZFAO approach [14], enabling us to compare the performance of these two methods. Custom software written in LabVIEW, 'Quartz', controlled the system and acquired the 2P images. The laser output from a 940 nm femtosecond laser

Optics EXPRESS

(Insight DeepSee, Spectral Physics) was reflected by a phase-only liquid crystal SLM (SLM1; HSPDM1920, Meadowlark Optics). The Bessel focus was generated by a Bessel module, which consisted of SLM1, a lens (L1; FL = 200 mm), and a transmissive annular mask. SLM1 was optically conjugated to the focal plane of the objective lens (dotted line, Fig. 1(a)), while the transmissive annular mask (chrome coating, Photo Sciences) was optically conjugated to the rear pupil plane of the objective lens (dashed line, Fig. 1(a)). When a concentric binary phase pattern with phase values 0 to π was displayed on SLM1, which was located at the front focal plane of L1, the light reflecting off SLM1 formed annular illumination at L1's back focal plane, where it was spatially filtered through the transmissive annular mask [8]. For our experiment, two transmissive annular masks were used to generate Bessel focus with 0.4-NA (inner diameter = 1.074 mm, outer diameter = 1.234 mm), FWHM of 43 μm, and 0.6-NA (inner diameter = 1.632 mm, outer diameter = 1.804 mm), FWHM of 23 μm. The optical field at the annular mask was then conjugated to the X and Y galvanometers (Galvo X and Y; 6215 H, Cambridge Technology) by a pair of relay lenses (L2-L3, FL = 750 mm and 350 mm; The telecentric f-θ lens pair conjugating Galvo X and Y were not shown in Fig. 1(a)). Galvo X and Y were conjugated to another SLM (SLM2; for implementing ZFAO and introducing artificial aberration into the system as detailed below) and the rear pupil plane of a 25×, 1.05 NA microscope objective (Olympus) by pairs of telecentric f-θ lenses (L4-L7, FL = 30 mm, 150 mm, 120 mm, and 240 mm; Special Optics). The annular electric field of the excitation laser at the objective pupil plane produced an axially extended Bessel focus at the objective focal plane. The emitted 2P fluorescence signal from the fluorophores was detected using a photomultiplier tube (H7422-40, Hamamatsu). For samples incorporating a cover glass, the correction collar of the microscope objective was adjusted for spherical aberration correction of the cover glass.

2.2. Aberration correction for Bessel-focus 2PFM using MFAO

The electric fields at the objective focal and pupil planes are related by Fourier transform (Fig. 1(b)). Hence, aberration correction can theoretically be accomplished either at the pupil plane or the focal plane (as well as their optically conjugated planes). For Bessel foci, correction at the focal plane is more effective. This is because although both Gaussian and Bessel foci are sensitive to phase error, Bessel foci are more susceptible to amplitude distortion than Gaussian foci and thus require correction in both phase and amplitude. However, available SLMs can control phase or amplitude but not both. To circumvent this limitation, applying phase correction using a phase-only SLM at the focal plane leads to both amplitude and phase modulations at the pupil plane, thus most effectively improving Bessel focal quality [14].

In our previous ZFAO approach [14], a zonal-based wavefront sensing method [19] was used to measure the phase aberration experienced by a Gaussian focus at the pupil plane with SLM2. The measured corrective phase pattern was then cropped by an annular mask and inverse Fourier-transformed to produce a pattern on SLM1 that both generated a Bessel focus and pre-shaped its wavefront for aberration correction. Although successful, this approach necessitates an additional Gaussian beam path. It also requires an SLM (i.e., SLM2) for wavefront sensing and another SLM (i.e., SLM1) for wavefront correction, and thus demands precise alignment between the two SLMs.

The MFAO method eliminates the need for the separate Gaussian beam path and the additional SLM. It utilizes the same optical elements as those in a conventional Bessel-focus 2PFM system. Conceptually, it is similar to earlier modal methods developed for Gaussian foci [21,22,28]. It introduces known aberration modes to the microscope and, for each mode, measures how a specific image quality metric (in this case, brightness) varies with the applied aberration mode coefficient. The final corrective wavefront is then obtained by summing the aberration modes with the coefficients that produce optimal image quality.

Optics EXPRESS

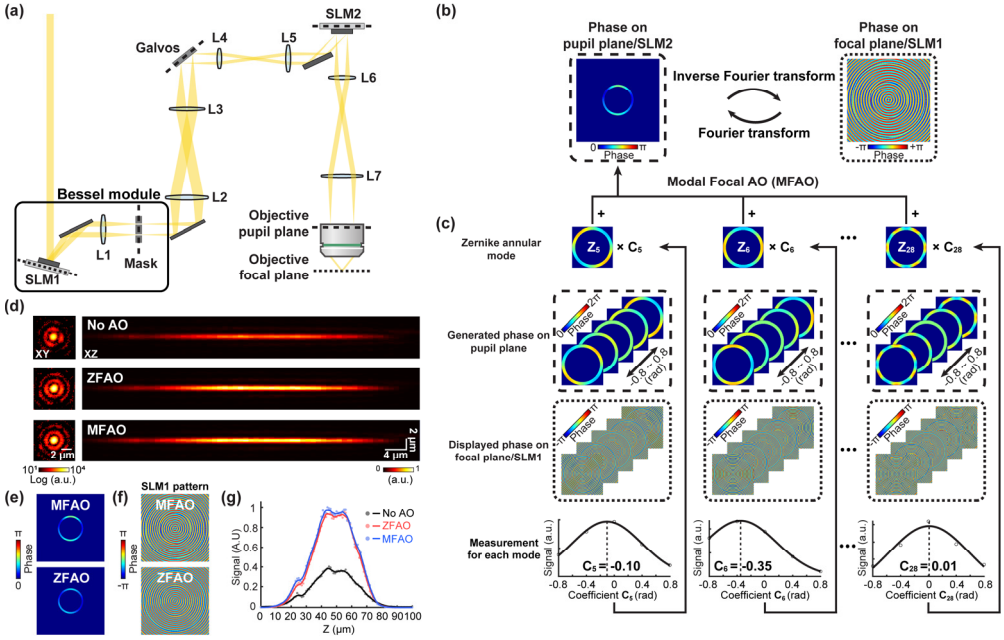

Fig. 1. Schematic of the optical setup and MFAO. (a) Optical setup for Bessel-focus 2PFM with MFAO. SLM1 is conjugated to the focal plane (dotted line) of the objective lens. Lens pairs (L2-L3, L4-L5, L5-L6) conjugate transmission annular mask, X and Y galvanometers, SLM2, and back pupil plane of the objective lens (dashed line). SLM1 (conjugated to objective focal plane): Generation of bias aberrations during aberration measurement and display of the final corrective phase pattern. SLM2 (conjugated to objective pupil plane): Zonal-based aberration measurement and introduction of artificial aberration to the system. (b) Relationship between the phases on the objective pupil plane/SLM2 and the objective focal plane/SLM1. Phase pattern at the focal plane (dotted line) is calculated by inverse Fourier transformation of the pupil-plane corrective phase within the annular mask (dashed line). (c) Workflow of aberration measurement in MFAO. Pupil-plane corrective phase is the linear superposition of Zernike annular modes Z_i with coefficients C_i. To determine C_i, bias aberrations of Z_i with coefficients from -0.8 rad to 0.8 rad (at 0.4 rad increments) at the pupil plane (dashed line) are generated by focal-plane SLM1 (dotted line) using the relationship in (b). Fitting the resulting fluorescent signal variation with a Gaussian function determines the C_i that maximizes signal for each mode Z_i. The pupil-plane corrective phase is calculated using C_i's and inverse Fourier transformed to obtain the final corrective phase on SLM1. (d) Lateral (in logarithmic scale) and axial (in linear scale) image of a 0.5-μm-diameter fluorescence bead imaged by a Bessel focus without AO, with ZFAO, and with MFAO, respectively. (e) Pupil-plane and (f) focal-plane/SLM1 corrective phase patterns from ZFAO and MFAO, respectively. (g) Axial signal profiles of images in (d). Post-objective power for (d): 45.2 mW. Wavelength: 940 nm. AU: arbitrary unit.

Unlike conventional modal AO methods, which typically utilize Zernike circular modes, MFAO decomposes phase aberrations into Zernike annular modes (top row, Fig. 1(c)), which form an orthogonal basis set for annular pupils [29–33]. Furthermore, instead of introducing these bias aberrations using a wavefront modulator at the pupil plane as in conventional modal AO, these modes are realized at the pupil plane by manipulating the phase pattern on SLM1, which is located at the focal plane and related to the pupil-plane phase pattern by Fourier transform (Fig. 1(b)).

Optics EXPRESS

During MFAO, to determine the optimal coefficient for each Zernike annular mode, we introduced bias aberrations of Zernike annular mode Z_i with coefficient varying from -0.8 rad to 0.8 rad at 0.4 rad increments (dashed box, Fig. 1(c)) by displaying the corresponding focal-plane phase pattern on SLM1 (dotted box, Fig. 1(c); calculated by inverse Fourier transforming the bias aberrations). Therefore, for each Zernike annular mode, five measurement points were used to determine the optimal correction coefficient. In total for N aberration modes, 5N measurements were acquired. We included the 5^{th} to 28^{th} Zernike annular modes but ignored Zernike annular modes with azimuthal indices $m = 0,1$ to which Bessel foci are insensitive (Supplement 1, Supplementary Note 1, Supplementary Fig. 1). Moreover, third-order astigmatism was also disregarded, because its high radial variation surpassed the achievable resolution of SLM1 (Supplement 1, Supplementary Note 2, Supplementary Fig. 2). As a result, a total of 16 Zernike annular modes were used for MFAO. With each SLM1 pattern, we acquired an image and calculated the mean pixel value of a target fluorescent object as the signal. To monitor photobleaching during the MFAO process, we tracked the mean pixel intensity of the image captured with zero amplitude bias aberration for each Zernike mode (i.e., 16 measurements for 16 Zernike modes investigated). For all the demonstrations presented in this paper, minimal photobleaching (<3%) was observed during aberration measurements. Fitting the signal versus Zernike annular mode coefficient with a Gaussian function (bottom row, Fig. 1(c)), we determined the coefficient C_i that maximized the fluorescent signal for each mode Z_i. We then linearly summed all the Zernike annular modes Z_i's with their coefficients C_i's to get the corrective wavefront at the pupil plane (dashed box, Fig. 1(b)), which was then inverse Fourier transformed to generate the final phase pattern to be displayed on SLM1 (dotted box, Fig. 1(b)) for Bessel focus generation and aberration correction.

2.3. Bead sample preparation

A solution of 0.5-μm diameter fluorescent beads (FluoSpheres Carboxylate-Modified Microspheres, yellow-green 505/515, ThermoFisher Scientific) was diluted and then pipetted onto microscope glass slides (12-550-12, Fisher Scientific) pre-coated with poly(L-lysine) hydrobromide (10 mg/mL; Sigma-Aldrich, P7890).

2.4. Zebrafish preparation and imaging

All animal experiments were conducted according to the National Institutes of Health guidelines for animal research. Procedures and protocols on mice and zebrafish were approved by the Institutional Animal Care and Use Committee at University of California, Berkeley (AUP-2020-06-13343).

Transgenic zebrafish *Tg(1020:Gal4; UAS:GtACR1-EYFP)* in a *nacre* -/- background at 1 and 2 days post-fertilization (dpf) were laterally mounted on a glass-bottom petri dish with 1.4% agarose dissolved in E3 media (Instant Ocean). The zebrafish were immobilized using tricaine during imaging.

2.5. Mouse preparation and imaging

Male and female Thy1-GFP line M transgenic mice (Jackson Laboratories, stock no. 007788, > 2 months old) were housed in cages (in groups of 1-5 before surgeries and in pairs or singly housed after) under a reverse light cycle.

Cranial window implantation procedures have been described previously [34]. Briefly, mice were anesthetized with isoflurane (1–2% by volume in oxygen) and given the analgesic buprenorphine (subcutaneously, 0.3 mg per kg of body weight). Animals were head fixed in a stereotaxic apparatus (Model 1900, David Kopf Instruments). A 3.5-mm-diameter craniotomy was created over the left visual cortex, leaving the dura intact. A glass window made of a single coverslip (Fisher Scientific No. 1.5) was embedded in the craniotomy and sealed in place

Optics EXPRESS

cyanoacrylate glue. Subsequently, a metal head-post was affixed to the skull using dental acrylic. *In vivo* imaging was conducted after at least 2 weeks of recovery. All imaging experiments were carried out on head-fixed anesthetized mice.

3. Results

3.1. MFAO corrects for aberrations of the microscope system

We first compared the effectiveness of MFAO with that of the previously developed ZFAO method for system aberration correction acquired using the signal of a 0.5-μm-diameter fluorescent bead. We measured the point spread functions (PSFs) of 0.4-NA Bessel foci before and after AO correction using the 0.5-μm-diameter fluorescence bead (Fig. 1(d)). We rendered the lateral (XY) PSF images in logarithmic scales to better visualize their side rings, which exhibited improved annular symmetry after both ZFAO and MFAO. We plotted the axial (XZ) PSF images in linear scales and observed signal increase after aberration correction. The pupil corrective phase pattern from MFAO closely matched that of ZFAO (Fig. 1(e)). By applying the phase patterns of their inverse Fourier transforms to SLM1 at the focal plane (Fig. 1(f)), both correction methods led to a 2.3-fold increase in peak signal (Fig. 1(g)). We also tested the performance of ZFAO and MFAO in correcting system aberrations for 0.5-NA Bessel foci (Supplement 1, Supplementary Note 3, Supplementary Fig. 3). Both ZFAO and MFAO led to similar signal enhancement. The signal improvement was more pronounced at 0.5 NA (Supplement 1, Supplementary Fig. 3c) than 0.4 NA (Fig. 1(g)), indicating a greater impact of aberration correction on higher-NA Bessel foci. From here on, system aberrations were always corrected for all images labeled as 'No AO'.

3.2. Artificial aberration correction using MFAO

Next, we investigated the effectiveness of our approach for correcting two aberrations artificially introduced at the pupil plane by displaying phase patterns of astigmatism (4^{th} Zernike circular mode under the OSA/ANSI indices) with a 0.36 wave root mean square (RMS) and trefoil (7^{th} Zernike circular mode under the OSA/ANSI indices) with a 0.6 wave RMS on SLM2. Astigmatism and trefoil were specifically chosen as artificial aberrations because Bessel foci are not sensitive to other common aberrations such as coma or spherical aberrations [14]. Conventional modal AO methods for Gaussian foci utilize standard Zernike modes, also referred to as Zernike circular modes, due to their orthogonality within a circular pupil [21,35]. However, these modes lose their orthogonality in an annular pupil, leading us to use Zernike annular modes instead. To confirm that Zernike annular modes are the correct basis set here, we also experimentally compared the performance of using Zernike annular modes versus Zernike circular modes.

Both astigmatism and trefoil ("Artificial aberration", Fig. 2(a),(d)) resulted in substantial distortions of the PSFs of 0.4-NA Bessel foci, diminishing the intensity of the central peak and redistributing energy to the side rings ("No AO", Fig. 2(b),(e)). MFAO using annular modes and signal from a fluorescent bead successfully restored the PSFs ("MFAO Annular", Fig. 2(b),(e)) to resemble the ones observed without artificial aberrations ("No aberration", Fig. 2(b),(e)) and recovered peak PSF signal to ~80% of the aberration-free condition (Fig. 2(c),(f)). In contrast, using Zernike circular modes, the corrective phase ("MFAO circular", Fig. 2(a),(d)) was inaccurate, incapable of restoring the shape of the PSFs ("MFAO Circular", Fig. 2(b),(e)) and further reducing its peak signal (Fig. 2(c),(f)).

Even with Zernike annular modes, MFAO did not fully recover the peak PSF signals for both artificial aberrations tested. This may be caused by two sources of error. The first source may be residual crosstalk between different Zernike annular modes in our intensity-based image metric. Such crosstalk has been previously shown to reduce aberration measurement accuracy in modal AO [28]. The second source of error comes from inaccuracies in the phase pattern generated by

Optics EXPRESS

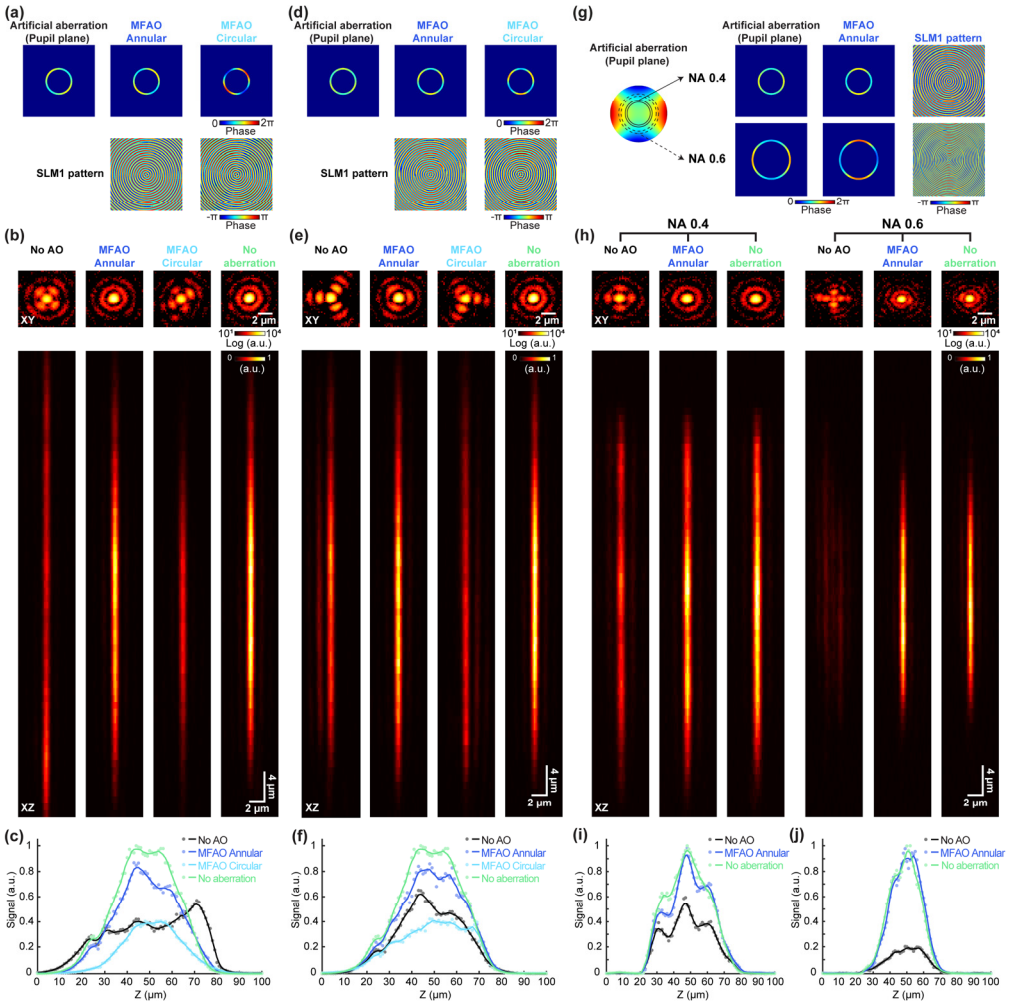

Fig. 2. MFAO corrects artificial aberration in fluorescence bead imaging. (a),(d) Artificial aberrations (astigmatism and trefoil), pupil-plane corrective phases, and focal-plane SLM1 phase patterns by MFAO using Zernike annular and circular modes, respectively. (b),(e) Lateral and axial Bessel-focus 2PFM image of a 0.5-μm-diameter fluorescence bead acquired without AO, with MFAO corrections in (a),(d) using Zernike annular and circular modes, respectively, and without artificial aberration. (c),(f) Axial signal profiles of images in (b),(e). (g) Illustration of artificial astigmatism affecting 0.4-NA (concentric circles) and 0.6-NA (concentric dashed circles) Bessel foci, pupil-plane corrective phases, and focal-plane SLM1 phase patterns by MFAO with Zernike annular modes for 0.4-NA and 0.6-NA Bessel foci, respectively. (h) Lateral and axial Bessel-focus 2PFM images of a 0.5-μm-diameter fluorescence bead acquired by 0.4-NA and 0.6-NA Bessel foci without AO, with MFAO corrections in (g), and without artificial aberration. (i),(j) Axial signal profiles of images in (h). Post-objective power: 37.4 mW for (b), 36.8 mW for (e), 68.5 mW for 0.4-NA (i), 48.6 mW for 0.6-NA (j). AU: arbitrary unit.

Optics EXPRESS

SLM1 due to its limited resolution and/or misalignment of optics. Together these factors led to residual phase errors of ~0.06 waves RMS after one iteration of MFAO correction.

We further assessed how Bessel foci of different NAs are affected by aberration. We introduced identical astigmatism with a 0.3 wave RMS (6th Zernike circular mode under the OSA/ANSI indices) at the pupil plane for Bessel foci of 0.4-NA or 0.6-NA, which had different annular ring diameters at the pupil plane thus distinct aberration profiles ("Artificial aberration", Fig. 2(g)). The 0.6-NA Bessel focus experienced more pronounced degradation in its PSF than the 0.4-NA focus ("No AO", Fig. 2(h)). MFAO with annular modes successfully restored the lateral and axial PSF profiles for both 0.4-NA and 0.6-NA ("MFAO Annular", Fig. 2(h)) to the ideal, aberration-free condition ("No Aberration", Fig. 2(h)), with almost complete peak signal recovery (Fig. 2(i),(j)). Given that this aberration had a more substantial impact on the 0.6-NA Bessel focus, the signal improvement brought about by AO was more pronounced (4.8×; compared with 1.6× for 0.4-NA focus). This result emphasizes the especially critical role of AO when employing higher-NA Bessel foci in imaging applications.

3.3. MFAO measures aberration accurately from images of neuronal processes in fixed brain slice

After confirming MFAO accurately measures aberrations from signals of fluorescence beads, we proceeded to demonstrate that it can measure aberration using the more complex signal of biological specimens. We introduced astigmatism (6^{th} Zernike circular mode under the OSA/ANSI indices) with a 0.45 wave RMS via SLM2 ("Artificial aberration", Fig. 3(a),(e)) and imaged fixed mouse brain slices (thickness: 40 μm; Thy1-GFP line M) at 30 μm depth with a 0.4-NA Bessel focus. Consistently over two different fields of view (FOVs), the aberrated Bessel focus led to lower resolution and image contrast, making it difficult to visualize neuronal processes ("No AO", Fig. 3(b),(f)).

Using fluorescence signal from neuronal structures over the entire FOV, MFAO acquired the corrective wavefront at the pupil plane ("Corrective phase", Fig. 3(a),(e)). From this point onward, the signal of neuronal structures was calculated as follows: We first median-filtered the image using a 3×3 pixel window; We applied intensity thresholding to the median-filtered image obtained under zero amplitude of bias aberration to create a segmentation mask for each Zernike mode. The threshold value for each Zernike mode was determined using the formula: mean + weight × std, where mean is the average pixel value within the entire image, and std is the standard deviation of the pixel values. The weight, typically between 1 and 2, was chosen via visual inspection to capture most of the neuronal structures. Then, we calculated the mean signal from the pixels within the segmented regions of the median-filtered images and used it as the value of the intensity metric. This mean signal was then used for aberration measurement in MFAO. Applying the corresponding corrective phase pattern to the focal plane ("SLM1 pattern", Fig. 3(a),(e)) resulted in images of enhanced signal intensity and improved spatial resolution ("AO (NA 0.4)", Fig. 3(b),(f)). Structures within two zoomed-in regions showed a substantial boost in image contrast and resolution after AO correction and up to 90% recovery of signal intensity of the aberration-free conditions (Fig. 3(c),(g)). In the spatial frequency domain, we also observed a substantial enhancement of the spectral power including in the high spatial-frequency band, indicative of resolution improvement (Fig. 3(d),(h)). Those results demonstrated that MFAO can correct aberration of Bessel foci using biological structures and substantially improve their image quality.

3.4. MFAO improves in vivo image quality of Bessel-focus 2PFM in zebrafish larvae

We next applied MFAO to *in vivo* imaging of YFP-expressing motor neurons in the spinal cords of *Tg(1020:Gal4; UAS:GtACR1-EYFP)* [36] zebrafish larvae. Sample-induced aberrations at the pupil plane were measured from images of the same motor neuron somata centering at 30

Optics EXPRESS

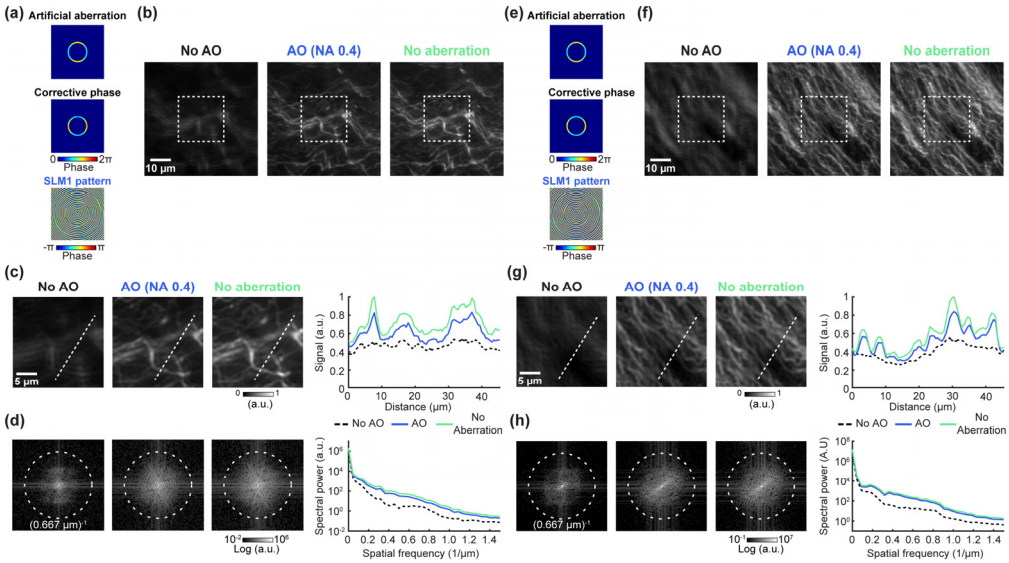

Fig. 3. MFAO on imaging of Thy1-GFP line M brain slices. (a),(e) Applied artificial astigmatism, pupil-plane corrective phase, and focal-plane SLM1 phase pattern for 0.4-NA Bessel focus by MFAO. (b),(f) Bessel-focus 2PFM images of the neuronal structures without AO, with AO correction in (a),(e), respectively, and without artificial aberration. Lateral pixel size: 0.5 μm. (c),(g) Zoomed-in images of white dashed boxes in (b),(f) (left) and signal profiles along white dashed lines (right). Lateral pixel size: 0.2 μm. (d),(h) Spectral power in the spatial frequency domain of the images in (c),(g) (left) and their radially averaged profiles (right). Dashed circle: $(0.667\ \mu m)^{-1}$. Post-objective power: 47.5 mW for (b),(c), 46.5 mW for (f),(g). AU: arbitrary unit.

μm depth for 0.4-NA and 0.6-NA Bessel foci ("Corrective phase", Fig. 4(a)). The MFAO was performed using fluorescence signals from segmented somata throughout the entire FOV. We then compared the motor neuron images acquired without and with the corresponding corrective patterns applied on SLM1 for each NA ("SLM1 pattern", Fig. 4(a)). Images acquired with 0.4-NA Bessel focus contained fluorescent puncta (Fig. 4(b)), which appeared blurrier in images acquired with 0.6-NA Bessel focus (Fig. 4(e)). This was caused by the higher proportion of energy allocated to the side rings in Bessel foci of higher NA [8]. We observed marginal improvement in resolution and signal for the image acquired with a 0.4 NA Bessel focus (Fig. 4(b)), with similar radially averaged profiles from spatial frequency space (Fig. 4(c)) and an up to 1.1-fold increase in signal after AO correction (Fig. 4(d)). More substantial improvements were observed for images acquired with a 0.6-NA Bessel focus (Fig. 4(e)), as evidenced by the increased magnitude of high-frequency components in the radially averaged profiles of spectral power (Fig. 4(f)) and a peak increase of 1.33-fold in signal with AO (Fig. 4(g)). The observation that *in vivo* image quality benefited more from aberration correction at higher NA aligns with our findings from fluorescent beads (Fig. 2(g)-(j)). Additional statistical analyses also support the significant resolution improvement at 0.6 NA (Supplement 1, Supplementary Note 4, Supplementary Fig. 4, Supplementary Table 1). In the following *in vivo* experiments, we used the 0.6-NA Bessel focus exclusively to demonstrate the impact of AO on image quality.

We further tested MFAO method on images of spinal cord motor neuron somata centering at 30 μm and axons centering at 50 μm in depth (Fig. 4(h),(i),(l)). AO correction consistently enhanced the high-frequency components of the radially averaged profiles of spectral power in the spatial frequency domain (Fig. 4(j),(m)). Comparing the line signal profiles of soma

Optics EXPRESS

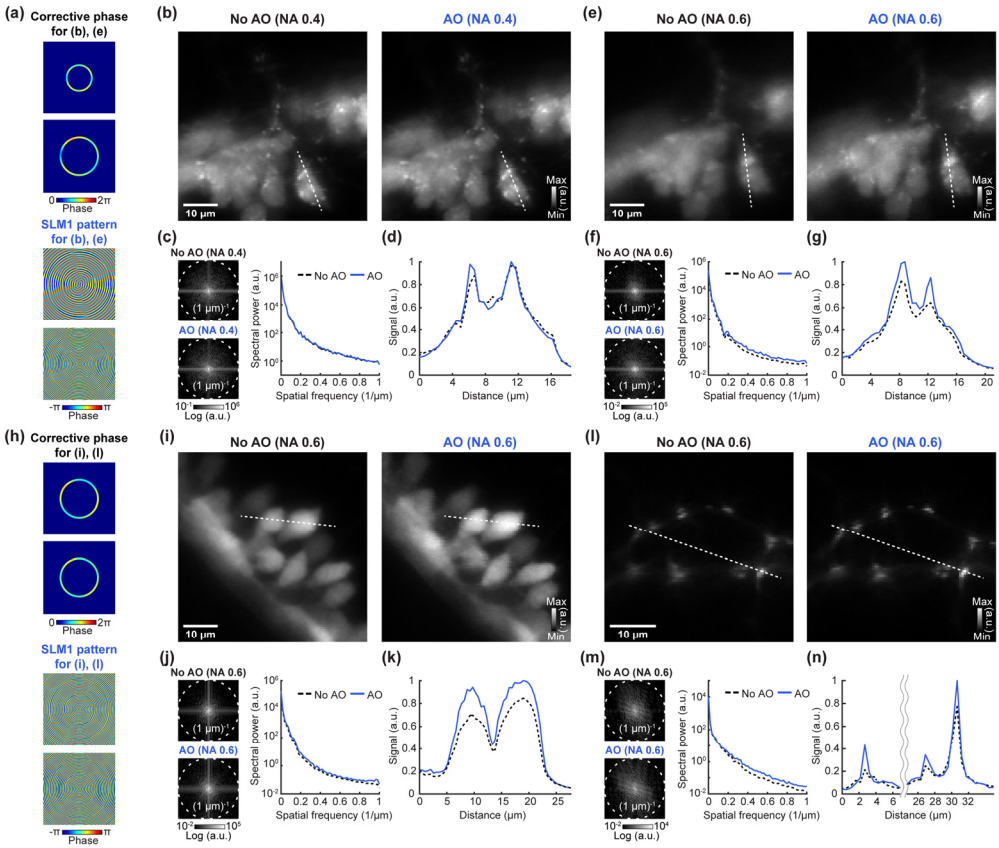

Fig. 4. MFAO application on in vivo imaging of zebrafish larvae. (a) Pupil-plane corrective phase and focal-plane SLM1 phase patterns for 0.4-NA and 0.6-NA Bessel foci by MFAO. (b),(e) Bessel-focus 2PFM images of spinal cord motor neuron somata acquired without and with AO corrections in (a) for 0.4-NA and 0.6-NA Bessel foci, respectively. Lateral pixel size: 0.5 μm. (c),(f) Spectral power in the spatial frequency domain of the images in (b),(e) (left) and their radially averaged profiles (right). Dashed circle: $(1\ \mu m)^{-1}$. (d),(g) Signal profiles along white dashed lines in (b),(e). (h) Pupil-plane corrective phase and focal-plane SLM1 phase patterns for 0.6-NA Bessel focus by MFAO. (i),(l) Bessel-focus 2PFM images of spinal cord motor neuron somata and axons acquired without and with AO corrections in (h) for 0.6-NA Bessel focus. Lateral pixel size: 0.5 μm. (j),(m) Spectral power in the spatial frequency domain of the images in (i),(l) (left) and their radially averaged profiles (right). Dashed circle: $(1\ \mu m)^{-1}$. (k),(n) Signal profiles along white dashed lines in (i),(l) (right). Post-objective power: 78.6 mW for (b), 52.9 mW for (e), 44.1 mW for (i), 50.5 mW for (l). AU: Arbitrary unit.

and axon structures, we observed a 1.3-fold improvement in signal of somata (Fig. 4(k)) and a 2-fold enhancement of axons (Fig. 4(n)). These findings demonstrate the effectiveness of MFAO in correcting aberrations of alive biological specimen and underscore its value for achieving high-resolution imaging.

3.5. *MFAO improves in vivo image quality of Bessel-focus 2PFM in the mouse cortex*

We further tested the performance of MFAO for high-resolution *in vivo* structural imaging of neuronal processes in the primary visual cortex of a Thy1-GFP-line M mouse. A cranial window made of No. 1.5 coverslip was installed above a craniotomy and precisely aligned to

Optics EXPRESS

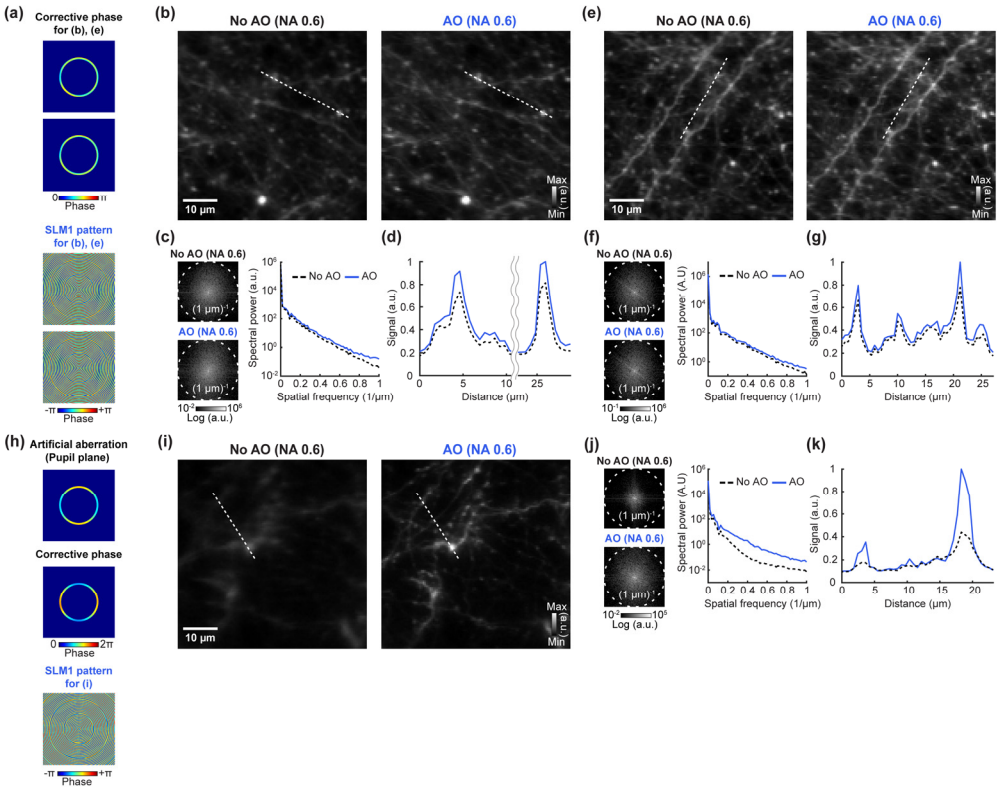

Fig. 5. MFAO application on in vivo imaging of Thy1-GFP line M mice. (a) Pupil-plane corrective phase and focal-plane SLM1 phase pattern for 0.6-NA Bessel focus by MFAO. (b),(e) Bessel-focus 2PFM images of dendritic structures acquired without and with AO correction in (a). Lateral pixel size: 0.5 μm. (c),(f) Spectral power in the spatial frequency domain of the images in (b),(e) (left) and their radially averaged profiles (right). Dashed circle: $(1\ \mu m)^{-1}$. (d),(g) Signal profiles along white dashed lines in (b),(e). (h) Applied artificial astigmatism, pupil-plane corrective phase, and focal-plane SLM1 phase pattern for 0.6-NA Bessel focus by MFAO. (i) Bessel-focus 2PFM images of dendritic structures acquired without and with AO correction in (h) for 0.6-NA Bessel focus. Lateral pixel size: 0.5 μm. (j) Spectral power in the spatial frequency domain of images in (i) (left) and their radially averaged profiles (right). Dashed circle: $(1\ \mu m)^{-1}$. (k) Signal profiles along white dashed lines in (i). Post-objective power: 48 mW for (b), 47.8 mW for (e), 47.5 mW for (i). AU: Arbitrary unit.

be perpendicular to the optical axis of microscope objective, enabling effective correction of spherical aberrations with correction collar [37]. Utilizing a 0.6-NA Bessel focus, we imaged dendritic structures located in two different FOVs at 70 μm beneath the dura. The sample-induced aberrations ("Corrective phase", Fig. 5(a)) were measured via MFAO using the mean signal of the dendritic structures across the entire FOV (Fig. 5(b),(e)). Applying the corrective pattern to SLM1 ("SLM1 pattern", Fig. 5(a)), we observed moderate improvement in resolution (Fig. 5(b),(e)), as indicated in the spatial frequency domain by the increased magnitude of high-frequency components in the radially averaged power spectral profiles (Fig. 5(c),(f)). Moreover, aberration correction led to an increase in fluorescence signal by up to 1.25-fold and 1.3-fold when comparing the line signal profiles of dendritic structures (Fig. 5(d),(g)).

Optics EXPRESS

The relatively modest improvement in image resolution could be attributed to the fact that Bessel foci are insensitive to spherical aberration or coma [14], which are the dominant aberration modes in superficial brain imaging. Our laser system did not have enough excitation power to probe deeper structures where aberrations are expected to be stronger and more complex [38]. To create a test for whether MFAO can correct for larger aberrations under *in vivo* imaging in mouse brain, we therefore introduced an artificial astigmatism (6^{th} Zernike circular mode under the OSA/ANSI indices) with a 0.25 wave RMS using SLM2 ("Artificial aberration", Fig. 5(h)). MFAO measured and corrected the combined effect of sample-induced and artificial aberrations using the mean signal of dendritic structures across the entire FOV centering at a depth of 140 μm ("Corrective phase", Fig. 5(h)). In the absence of AO, dendritic structures were poorly resolved. Applying the focal correction pattern to SLM1 ("SLM1 pattern", Fig. 5(h)), we observed a substantial enhancement in resolution, signal, and contrast (Fig. 5(i)). There was a marked increase in the magnitude of the high-frequency components in the radially averaged profile of spectral power in the spatial frequency domain (Fig. 5(j)). Aberration correction also led to a 2.3-fold enhancement in the signal of the fine dendritic structures (Fig. 5(k)). These findings substantiate that MFAO can effectively correct even severe aberrations using complex neuronal structures *in vivo*.

4. Discussions

Bessel-focus 2PFM is a valuable microscopy technique for volumetric imaging of biological samples. While a prior study has introduced a zonal AO approach to correct for aberrations experienced by Bessel foci [14], it requires two SLMs, one placed in the objective pupil plane to measure the aberration experienced by a Gaussian focus and the other placed in the objective focal plane to correct for the aberration. Here, we developed a modal AO approach that is specifically conceived for Bessel-focus 2PFM. Utilizing only one SLM placed in conjugation with the objective focal plane to generate different Zernike annular modes in the objective pupil plane and measuring their effects on fluorescent signal, our MFAO approach achieved precise aberration measurement and correction for both artificial aberration and biological-sample-induced aberrations. Unlike the previous zonal method [19] used in ZFAO, which requires isolated fluorescent structures for aberration measurement, our approach can measure aberration from fluorescent signal of complex structures, broadening the wavefront sensing applicability to general biological samples. We demonstrated substantial benefit of AO in high-resolution imaging applications in fluorescent beads, mouse brain slices, as well as in zebrafish larvae and mouse cortical structures *in vivo*.

In current MFAO implementation, the image acquisition time for each Zernike mode was 7.5 s (1.5 s per measurement point, with 5 measurement points) and overall time, including overhead in the image acquisition program for each Zernike mode, was 10 s. Consequently, the actual image acquisition time required for the correction of 16 Zernike modes was 120 s, which for brighter samples can be further reduced. The total experimental time included pauses between different bias aberrations and was 240 s. As aberration profiles in biological samples typically do not change rapidly, this aberration measurement time was fast enough for *in vivo* imaging. Further reductions in acquisition time could be achieved by optimizing the image acquisition software and the synchronization between imaging and SLM control.

The performance of MFAO can be further enhanced in terms of aberration measurement accuracy. In our demonstrations, MFAO was applied for one iteration only. Correcting larger aberrations that exceed the range of bias aberrations could be achieved through additional iterations of MFAO. Alternatively, adapting the bias aberration magnitude based on the severity of the aberration—reducing it for smaller aberrations and increasing it for larger aberrations—could improve the accuracy of aberration measurements. Finally, while photobleaching was monitored and found to be minimal for our samples during MFAO, the risk of photobleaching reducing

Optics EXPRESS

aberration measurement accuracy may be minimized by using image sharpness as the image metric [39] instead of brightness.

To our knowledge, this is the first modal AO approach for Bessel foci utilizing Zernike annular modes, instead of the more commonly applied Zernike circular modes for Gaussian foci. This MFAO approach can be generally applied to microscopy modalities in which Bessel foci are utilized [40,41]. Furthermore, the principle behind our technique—using a tailored orthogonal basis within the pupil plane, implemented via an SLM at the focal plane—may be adapted for other microscopy modalities featuring a non-circular pupil, such as lattice-light sheet microscopy [42,43]. The simplicity and efficiency of the MFAO approach could significantly impact a wide range of biological applications by facilitating the integration of AO into diverse microscopy modalities.

Funding. National Institutes of Health (U01NS118300, 1R01NS107506); U.S. Department of Energy (DE-SC0021986).

Acknowledgments. We thank Dr. Karl Deisseroth and Dr. Suresh Jesuthasan for generously providing the *Tg(1020:Gal4; UAS:GtACR1-EYFP)* fish line.

Disclosures. The Bessel focus scanning (N.J.) intellectual property has been licensed to Thorlabs Inc. by the Howard Hughes Medical Institute. The remaining authors declare no competing interests.

Data availability. Data underlying the results presented in this paper are not publicly available at this time but may be obtained from the authors upon reasonable request.

Supplemental document. See Supplement 1 for supporting content.

References

1. W. Denk, J. H. Strickler, and W. W. Webb, "Two-photon laser scanning fluorescence microscopy," Science **248**(4951), 73–76 (1990).
2. F. Helmchen and W. Denk, "Deep tissue two-photon microscopy," Nat. Methods **2**(12), 932–940 (2005).
3. N. Ji, J. Freeman, and S. L. Smith, "Technologies for imaging neural activity in large volumes," Nat. Neurosci. **19**(9), 1154–1164 (2016).
4. W. T. Welford, "Use of annular apertures to increase focal depth," J. Opt. Soc. Am. **50**(8), 749–753 (1960).
5. E. J. Botcherby, R. Juškaitis, and T. Wilson, "Scanning two photon fluorescence microscopy with extended depth of field," Opt. Commun. **268**(2), 253–260 (2006).
6. G. Thériault, Y. De Koninck, and N. McCarthy, "Extended depth of field microscopy for rapid volumetric two-photon imaging," Opt Express **21**(8), 10095–10104 (2013).
7. G. Thériault, M. Cottet, A. Castonguay, *et al.*, "Extended two-photon microscopy in live samples with Bessel beams: steadier focus, faster volume scans, and simpler stereoscopic imaging," Front. Cell. Neurosci. **8**, 139 (2014).
8. R. Lu, W. Sun, Y. Liang, *et al.*, "Video-rate volumetric functional imaging of the brain at synaptic resolution," Nat. Neurosci. **20**(4), 620–628 (2017).
9. A. Song, A. S. Charles, S. A. Koay, *et al.*, "Volumetric two-photon imaging of neurons using stereoscopy (vTwINS)," Nat. Methods **14**(4), 420–426 (2017).
10. R. Lu, M. Tanimoto, M. Koyama, *et al.*, "50 Hz volumetric functional imaging with continuously adjustable depth of focus," Biomed Opt Express **9**(4), 1964–1976 (2018).
11. R. Lu, Y. Liang, G. Meng, *et al.*, "Rapid mesoscale volumetric imaging of neural activity with synaptic resolution," Nat. Methods **17**(3), 291–294 (2020).
12. G. Meng, Y. Liang, S. Sarsfield, *et al.*, "High-throughput synapse-resolving two-photon fluorescence microendoscopy for deep-brain volumetric imaging in vivo," Elife **8**, e40805 (2019).
13. J. L. Fan, J. A. Rivera, W. Sun, *et al.*, "High-speed volumetric two-photon fluorescence imaging of neurovascular dynamics," Nat. Commun. **11**(1), 6020 (2020).
14. W. Chen, R. G. Natan, Y. Yang, *et al.*, "In vivo volumetric imaging of calcium and glutamate activity at synapses with high spatiotemporal resolution," Nat. Commun. **12**(1), 6630 (2021).
15. N. Ji, "Adaptive optical fluorescence microscopy," Nat. Methods **14**(4), 374–380 (2017).
16. M. J. Booth, "Adaptive optical microscopy: the ongoing quest for a perfect image," Light:Sci. Appl. **3**(4), e165 (2014).
17. K. M. Hampson, R. Turcotte, D. T. Miller, *et al.*, "Adaptive optics for high-resolution imaging," Nat. Rev. Methods Primers **1**(1), 68 (2021).
18. Q. Zhang, Q. Hu, C. Berlage, *et al.*, "Adaptive optics for optical microscopy," Biomed. Opt. Express **14**(4), 1732–1756 (2023).
19. N. Ji, D. E. Milkie, and E. Betzig, "Adaptive optics via pupil segmentation for high-resolution imaging in biological tissues," Nat. Methods **7**(2), 141–147 (2010).

Optics EXPRESS

20. R. Liu, D. E. Milkie, A. Kerlin, *et al.*, "Direct phase measurement in zonal wavefront reconstruction using multidither coherent optical adaptive technique," Opt. Express **22**(2), 1619–1628 (2014).
21. M. J. Booth, M. A. A. Neil, R. Juškaitis, *et al.*, "Adaptive aberration correction in a confocal microscope," Proc. Natl. Acad. Sci. U.S.A. **99**(9), 5788–5792 (2002).
22. D. Débarre, E. J. Botcherby, T. Watanabe, *et al.*, "Image-based adaptive optics for two-photon microscopy," Opt. Lett. **34**(16), 2495–2497 (2009).
23. I. N. Papadopoulos, J.-S. Jouhanneau, J. F. A. Poulet, *et al.*, "Scattering compensation by focus scanning holographic aberration probing (F-SHARP)," Nat. Photonics **11**(2), 116–123 (2017).
24. Q. Hu, M. Hailstone, J. Wang, *et al.*, "Universal adaptive optics for microscopy through embedded neural network control," Light:Sci. Appl. **12**(1), 270 (2023).
25. K. Wang, W. Sun, C. T. Richie, *et al.*, "Direct wavefront sensing for high-resolution in vivo imaging in scattering tissue," Nat. Commun. **6**(1), 7276 (2015).
26. C. Wang, R. Liu, D. E. Milkie, *et al.*, "Multiplexed aberration measurement for deep tissue imaging in vivo," Nat. Methods **11**(10), 1037–1040 (2014).
27. Y. N. Sulai and A. Dubra, "Non-common path aberration correction in an adaptive optics scanning ophthalmoscope," Biomed. Opt. Express **5**(9), 3059–3073 (2014).
28. A. Facomprez, E. Beaurepaire, and D. Débarre, "Accuracy of correction in modal sensorless adaptive optics," Opt. Express **20**(3), 2598–2612 (2012).
29. K. Niu and C. Tian, "Zernike polynomials and their applications," J. Opt. **24**(12), 123001 (2022).
30. V. N. Mahajan, "Zernike annular polynomials for imaging systems with annular pupils," J. Opt. Soc. Am. **71**(1), 75–85 (1981).
31. V. N. Mahajan, "Zernike annular polynomials and optical aberrations of systems with annular pupils," Appl. Opt. **33**(34), 8125–8127 (1994).
32. G. Dai and V. N. Mahajan, "Zernike annular polynomials and atmospheric turbulence," J. Opt. Soc. Am. A **24**(1), 139–155 (2007).
33. X. Hou, F. Wu, L. Yang, *et al.*, "Comparison of annular wavefront interpretation with Zernike circle polynomials and annular polynomials," Appl. Opt. **45**(35), 8893–8901 (2006).
34. W. Sun, Z. Tan, B. D. Mensh, *et al.*, "Thalamus provides layer 4 of primary visual cortex with orientation-and direction-tuned inputs," Nat. Neurosci. **19**(2), 308–315 (2016).
35. Q. Hu, J. Wang, J. Antonello, *et al.*, "A universal framework for microscope sensorless adaptive optics: Generalized aberration representations," APL Photonics **5**(10), 100801 (2020).
36. G. A. Mohamed, R.-K. Cheng, J. Ho, *et al.*, "Optical inhibition of larval zebrafish behaviour with anion channel-rhodopsins," BMC Biol. **15**(1), 103 (2017).
37. R. Turcotte, Y. Liang, and N. Ji, "Adaptive optical versus spherical aberration corrections for in vivo brain imaging," Biomed. Opt. Express **8**(8), 3891–3902 (2017).
38. N. Ji, T. R. Sato, and E. Betzig, "Characterization and adaptive optical correction of aberrations during in vivo imaging in the mouse cortex," Proc. Natl. Acad. Sci. U.S.A. **109**(1), 22–27 (2012).
39. D. Débarre, M. J. Booth, and T. Wilson, "Image based adaptive optics through optimisation of low spatial frequencies," Opt. Express **15**(13), 8176–8190 (2007).
40. R. Lu, N. Aguilera, T. Liu, *et al.*, "In-vivo sub-diffraction adaptive optics imaging of photoreceptors in the human eye with annular pupil illumination and sub-Airy detection," Optica **8**(3), 333–343 (2021).
41. T. A. Planchon, L. Gao, D. E. Milkie, *et al.*, "Rapid three-dimensional isotropic imaging of living cells using Bessel beam plane illumination," Nat. Methods **8**(5), 417–423 (2011).
42. T.-L. Liu, S. Upadhyayula, D. E. Milkie, *et al.*, "Observing the cell in its native state: Imaging subcellular dynamics in multicellular organisms," Science **360**(6386), eaaq1392 (2018).
43. B.-C. Chen, W. R. Legant, K. Wang, *et al.*, "Lattice light-sheet microscopy: imaging molecules to embryos at high spatiotemporal resolution," Science **346**(6208), 1257998 (2014).